RUHR UNIVERSITÄT BOCHUM

RUB

Ruhr-Universität Bochum
Fakultät für Physik und Astronomie

Patrick Kleu, 108021263723
Leonard Kosziol, 108017216753

Observational Astronomy

Supervisor: Dr. Vandad Fallah Ramazani

Date of submission: March 11, 2023

Contents

List of Figures

List of Tables

1 Introduction

In 1949 the astronomers William Hiltner and John S. Hall first observed the polarization of starlight. After that, several theories were created to explain this polarization. At the source, the heat radiation cannot be polarized, but interstellar dust aligned through a magnetic field or dusty disks around the star itself are able to polarize radiation [1], [?]. The polarization observed in known standard stars can be used to calibrate for other polarization measurements, as the polarization of stars can be well measured. In this lab course, the polarization of five different sources is measured with the LAST-telescope prototype located at the Ruhr-Universität Bochum. This telescope is used later on for survey-like monitoring of **BL-Lacertae-Objects**. These **BL-Lac** objects are types of active galactic nuclei (AGN), less luminous than quasars but still known to be some of the most luminous objects known. The light emitted by these objects is polarized with a polarization degree up to 20 %. In this lab course, the telescope is used to determine the polarization degree and polarization angle of different celestial objects. In this lab course, a LAST-Prototype setup is used to get familiar with observational astronomy and doing first measurements of polarization parameters. Basics of data reduction, calibration, data analysis as well as the set up and observation procedure are introduced and solidified. In the following, the theoretical background on optical polarization is given. Furthermore, the basic procedure of data analysis and image reduction is introduced. The setup and the used telescope are described briefly and observation procedure is outlined. At last, the first measurements are presented and discussed.

2 Image sensors in astronomy

Figure 1: An example CMOS sensor used for astrophotography. [3]

To take images in astronomy CCD-sensors are commonly used. CCD is short for *charge-coupled-device*. A CCD's functionality is based on the inner photo-effect. The main ingredients to construct such a sensor are photodiodes, aligned in an array, most of the time rectangular or square. The size of each diode determines both the light sensitivity and the the resolution at a given sensor size. The bigger each diode, the higher the sensitivity and the lower the resolution. Most of the time, CCD's are metal insulator semiconductor structures. During exposure, the incoming photons transfer their energy onto the electrons in the semiconductor. This leads to both negative charged, free electrons and positive charged "holes". Due to an outer current, the electrons and the holes are separated. The charges are stored in a potential well similar to a capacitor. The charge stored is directly proportional to the amount of light.

At this point, the effect of "blooming" can occur. Blooming occurs when one potential well is over-filled, resulting in charges being "spilled" in surrounding potential wells, mostly the wells which are coupled for the readout procedure. Blooming can be seen on pictures as highly overexposed stripe. After the exposure the charges are moved one after another until they reach the the readout amplifier, where the charge packets are converted to a charge-dependent electric voltage, which then again can be translated to a digital signal. The construction of the image is therefore serial, whereas the exposure was parallel with all pixels being exposed at the same time.

On the contrary, CMOS-sensors (Complementary metal-oxide-semiconductor) use a "rolling shutter" exposure, where the pixels are exposed line after line. This is a disadvantage when taking pictures of fast-moving objects, which is not the case in most of astronomy. Unlike for CCD's, in CMOS-sensors each pixel has its own amplifier and analog to digital-converter. The signal is then directed to a readout-circuit, which is often one readout per row of pixels. One pixel is called active pixel sensor (APS) and consists at least of a photodiode, a capacitor to collect the charge, an amplifier and the dataline for read out, a analog-digital converter directly at the APS is optional. For a long time, the space for one pixel in a CMOS-sensor was a lot bigger than in CCD's, as each pixel had more electronic parts than in CCD's, resulting in less resolution for the same sensor size. As each pixel is read out separately, in CMOS-sensors blooming is much less likely to occur, as the pixels are not coupled as they are in CCD's. Furthermore, pixel-binning and readout are easier and faster for CMOS-sensors. It is possible to select only part-images of the whole sensor without exposing the whole sensor first.

In comparison, using a CMOS-sensor yields cheaper production, easier and faster data read-out and less power consumption than CCD's [4]. These aspects are the main reasons why the LAST-telescopes will use CMOS-sensors. A disadvantage of CMOS sensors is the poor quantum efficiency [5], resulting in less sensitivity than a CCD. This disadvantage can be accepted in the case for the LAST survey, as a lot of sensors are needed for the survey and the cost needs to be reduced as much as possible.
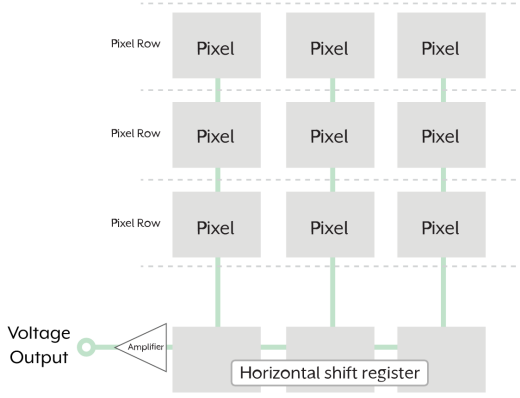
Figure 2: Block diagram of a CCD sensor, taken from `https://thinklucid.com/tech-briefs/understanding-digital-image-sensors/`
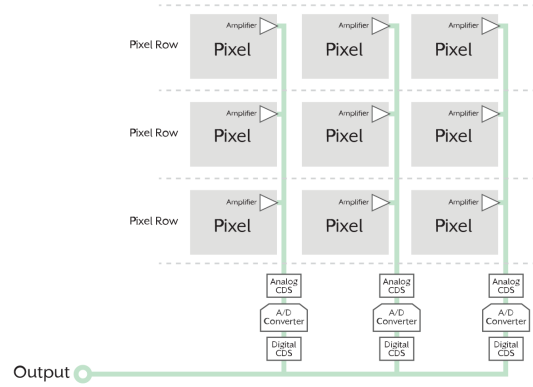
Figure 3: Block diagram of a CMOS sensor, taken from `https://thinklucid.com/tech-briefs/understanding-digital-image-sensors/`

3 Polarization in astronomy

In this experiment, we are looking at polarized optical emission from point sources like stars or AGNs. There are other types of polarized emission like, e.g., synchrotron emission, but the focus of this introduction will be on the ones relevant for the sources observed during the lab course. The explanations in this chapter and its subsections follow [7], if not indicated otherwise.

The optical emission of stars is not polarized *a priori*, but the polarization degree increases due to propagation effects like differential absorption when passing through the interstellar medium or from scattering of radiation. In both cases, there must be an anisotropy in the optical medium the light has to travel through.

In comparison to photometry, polarization is measured more easily in a sense that high precision can be achieved and that there is no calibration needed. For one, the earth's atmosphere does not change the state of polarization of the incident starlight [8]. Furthermore, it is a differential measurement, because the light intensity of two basis states in polarization of the same source are compared to one another, eliminating the need for calibration. In general, this is done by passing the light through a device that splits up the two polarization states, so that the light intensities of both can be measured separately by some detector. The states can be measured one after the other or even simultaneously, if the measurement apparatus is equipped with the right kind of polarizing prism. In our experiment, we use a rotating polarization filter and image the sky after the light has passed through it with an image sensor, measuring the different states one after the other indirectly, i.e. using Stokes parameters.

3.1 Interstellar polarization

One type of polarization to be expected when imaging stars in the Milky Way is interstellar polarization, which is increasing with distance to the source and is connected to interstellar extinction. It is created by dielectric dust grains with a typical size around $100\,\mathrm{nm}$. These attenuate and redden the radiation, as well as produce polarization by absorption, which can only happen if they have a preferred axis of alignment. A key process in producing this aligment is called radiative torque alignment (RAT). This mechanism is based on the presence of external magnetic fields and the dust grains themselves being elongated and paramagnetic. Because of the latter property, they have an individual magnetic moment, so that a precession movement can be induced by the different circular polarization components of incoming light.
The precession causes a stable or constant orientation when averaged over time. The effect of linear polarization is then explained because light is preferentially absorbed about the long axis (there is more matter to absorb in this direction), so that the residual radiation is polarized about the short

axis. A common term for this process is dichroic absorption. With radiative torque alignment, the short axis or the dust grains will tend to align with the magnetic field. This means that, in contrast to synchrotron radiation, optical emission will be polarized parallel to the interstellar magnetic field. Note that this is independent from the mechanism that causes the orientation of the grains.

The wavelength dependence of interstellar polarization towards virtually all stars can be well described with only two parameters, the wavelength of maximum polarization $\lambda_{\max}$ and the value of the maximum polarization, $P_{\max}$. The function used to fit the datapoints is known as the Serkowski curve and has the form

$$P(\lambda) = P_{\max} \exp(-1.15 \ln^2[\lambda_{\max}/\lambda])$$

. $P_{\max}$ depends on the number of dust grains and how well the are aligned. $\lambda_{\max}$ usually ranges from $300\,\mathrm{nm}$ to $800\,\mathrm{nm}$, being $550\,\mathrm{nm}$ on average. Furthermore, is interesting that the polarization curve and the extinction curve do not always have the same structure. For example, the extinction curve can have features the polarization curve is lacking. Comparing such features, it can, i.e., be concluded that graphitic carbon particles are not aligned, since their impact is only visible in extinction.

Moving to longer wavelengths and/or larger temperatures of the grains, the emissive component of the radiation can be larger than the absorbed component. This means that the net polarization from the grains is now perpendicular to the ambient magnetic field. Practical examples of this principle being used for observations are mapping the magnetic field of (cold) dust clouds at (sub)millimetre wavelengths or the magnetic fields in the Sgr A region near the Galactic centre at mid-infrared wavelengths, because the grains are relatively warm themselves there. Usually, it is only possible to map the projection of the magnetic field vector onto the line of sight or onto the sky plane, depending on whether the emissive or absorbing polarization is dominant. Under special conditions like those near the galactic center, even the angle between the line of sight and the magnetic field vector can be measured, allowing for a three-dimensional reconstruction [7].

3.2   Polarization through scattering

In addition to interstellar polarization, where the light is polarized on its way through the interstellar medium, it can happen that the source of polarization is at the very same position as the star. Typically, dust particles around a (young) star will be arranged in the form of a disk. More specifically, this can be a protoplanetary disk or a debris disk that is formed from the collisions of planets or other orbital bodies. Such disks were first discovered by the IRAS satellite that launched in 1983 [11]. It was found that some bright nearby stars such as Vega and Fomalhaut show an excess of infrared radiation, meaning they emitted more power between $25\,\mu\mathrm{m}$ and $100\,\mu\mathrm{m}$ than would have been possible only with their photospheres [11]. It is thought that this happens because of dusty circumstellar disks, which absorb optical ultraviolet light from the star and re-emit it in the infrared [11]. Accordingly, many studies of dusty disks have relied on using infrared regions of the spectrum, employing, e.g., the NICMOS camera of HST or the airborne infrared observatory SOFIA [11]. However, millimetre and submillimetre observations also provide valuable information, such as detecting emission lines from molecules that are helpful to understand the chemistry of the formation of planetary systems [11]. Furthermore, the angular resolution of interferometers such as ALMA is high enough to actually image such objects in good detail [11]. See fig. 9 for a selection. Fig. 4 also provides a good idea of the size of such disks in comparison to the solar system. These observations have very little to do with optical polarization, but nonetheless they allow to associate disks and their host stars. This made clear that, without any surprise, dusty disks are hosted by relatively young stars around 10-100 Myrs of age [11]. This means they are a phenomenon of the formative phase of planetary systems (respectively the mutual destruction of minor bodies such as asteroids) and early main-sequence evolution [11]. Note that in the earlier T TAURI-phase the dust is already there, but so is the gas that forms the star, before it is eventually driven away by the radiation when nuclear fusion becomes efficient [11].

Coming back to polarization, the polarization angle will then be perpendicular to the disk and the fractional polarization will depend on its inclination. Some hints of this can be spotted in fig. 10. The size of the scatterers can be inferred from the wavelength dependence of the fractional polarization, which is connected to the possibility to study the formation of planetary systems with such observations, as the disks are substantially more easily observed than the planets or planetary bodies themselves.

In addition, stellar disks can be imaged with the means of polarization. On the one hand, it is possible to remove the intense light from the star by making an image only of polarized intensity, leaving out the unpolarized part. This makes it possible to observe ejected material near the star, the so-called protoplanetary disk, which is way fainter, however substantially higher polarized then the light from the star. Note that "planetary" is meant to refer to a planetary nebula that is created after a supernova explosion, but has nothing to do with a system of orbital bodies like planets. Furthermore, comparisons of polarized and total flux are used to observe a source from different angles. This works because the polarized part of the radiation is scattered by an object near the source, so one can "see" (but not necessarily image) the source from the viewpoint of that object. Such scatterers can include electron clouds in the case of AGNs or the formerly mentioned disks around stars. Note that this is independent from the degree of obscuration of the source.

Using spectropolarimetry, one can even infer the geometries (in relation to the observer) and velocity structures of, e.g., disks around stars. This enables spatial "resolutions" far beyond the reach of optical interferometers.

There is even a technique to image exoplanets near the star which relies on polarization measurements. This can reduce the atmospherically induced speckle noise so much that a planet becomes visible. Normally, a planet or a circumstellar disk that is far enough away from its host star to be individually resolved with the respective telescope would be hidden in the speckle halo of the star, which only happens because of refraction of the starlight in the earth's atmosphere. However, it is possible to image the star with a dual-beam polarimeter (the images have to be taken exactly simultaneously) and make a difference image from orthogonal polarizations. This way, the speckled halo is exactly substracted and what remains is an image of the surroundings of the star in polarization.

However, a star (or an AGN) does not have to be placed inside a disk, but thicker tori (geometrically and optically) or even dusty envelopes which fully contain the central object are also possible. For a star, this typically happens during its formation. Generally, such structures can be so thick optically that the central object behind them becomes invisible. However, there are often outflows along its rotation axis, which produce a cavity in the dust structure where the optical depth is reduced drastically. Escaping photons from the source can then be back-scattered and form reflection nebulae. This happens with stars as well was for AGNs. The geometry of AGNs can be well inferred using polarimetric methods: from the polarization pattern in the reflection nebula, one can infer the position of the source, from the difference in polarization of the lobes the inclination of the disk and outflows and the wavelength dependence again provides information about the scatterers. However, this is not the primary domain of the LAST-telescope, since the sources must be resolved and exposures have to be sufficiently long.

Furthermore, the so-called polarized flux spectrum (flux spectrum times polarization spectrum) played an important role in establishing the unified model of AGNS. More specifically, it demonstrated that there are indeed both broad and narrow emission lines for many AGNS, eventhough just one category was prevalent in the total flux spectrum. This was a clue for concluding that the broad line emission regions near the central engine were just obscured by an optically thick dusty torus for many lines of sight.
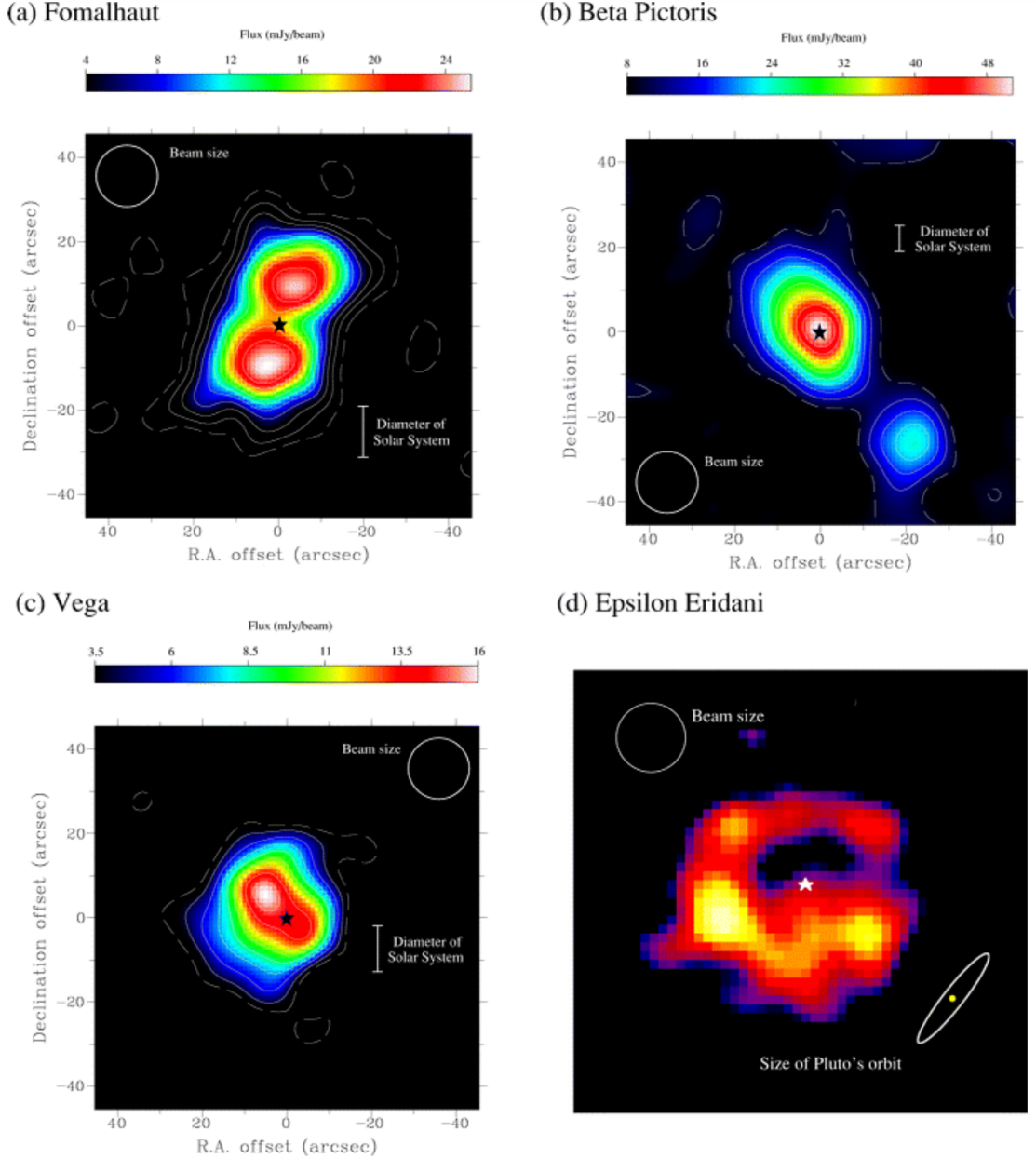
Figure 4: Circumstellar disks around nearby stars imaged with the SCUBA bolometer array on the James Clerk Maxwell telescope at $850\,\mu$m. Positions of the host stars are indicated with black little star symbols. North is up and East is to the left. Images courtesy of W. Holland. Taken from [11].

4 The case for the LAST telescope

4.1 Quantifying the scientific output of survey telescopes

The concept of the LAST telescope, that is to have many small off-the-shelf telescopes survey the sky at one observatory site, is motivated by considerations on how to maximize the scientific output of a survey telescope while minimizing the financial costs. To properly plan an observatory and to realize which characteristics are actually needed to meet scientific goals, different formulae have been developed to compare the presumed scientific output of different telescope setups depending on their properties.

All of them are measures of how many (possibly transient) sources can be detected per time by the individual telescope respectively by an observatory hosting several identical telescopes. The
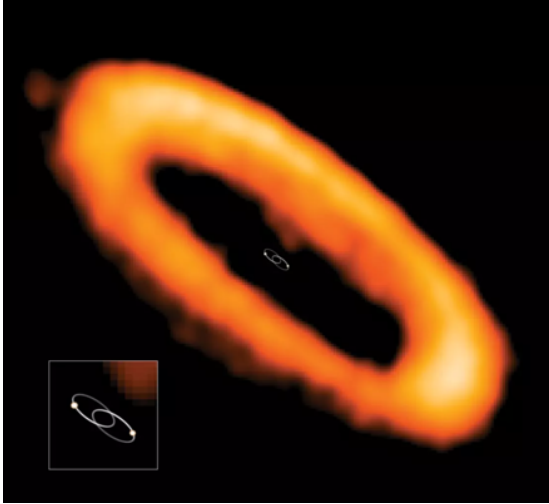
Figure 5: AK Scorpii. Note the size of the binary system indicated in the middle.
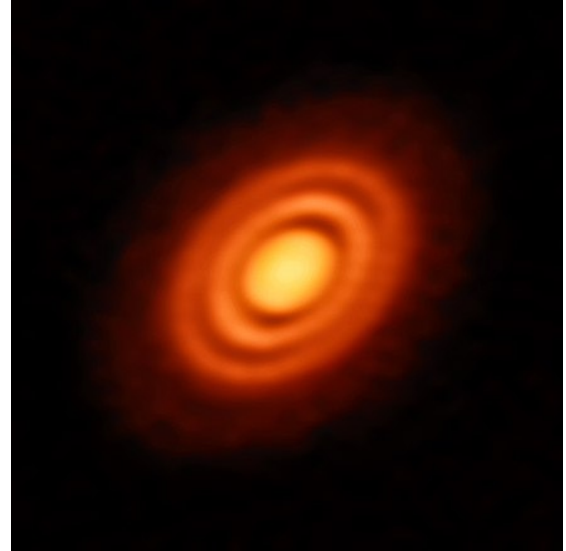
Figure 6: Primordial cloud of gas and dust around HD163296
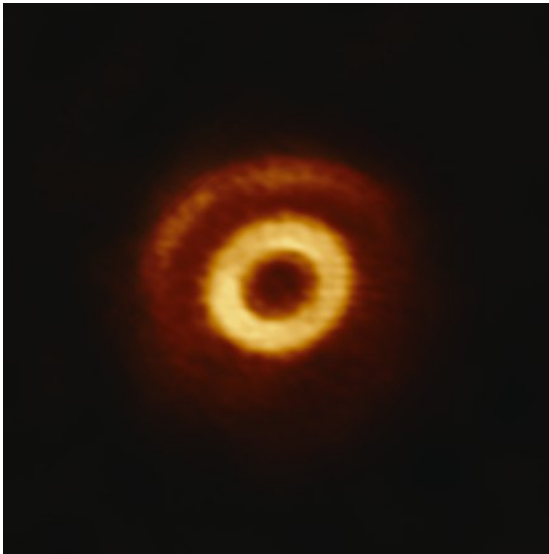
Figure 7: Ring around V1247A Orionis
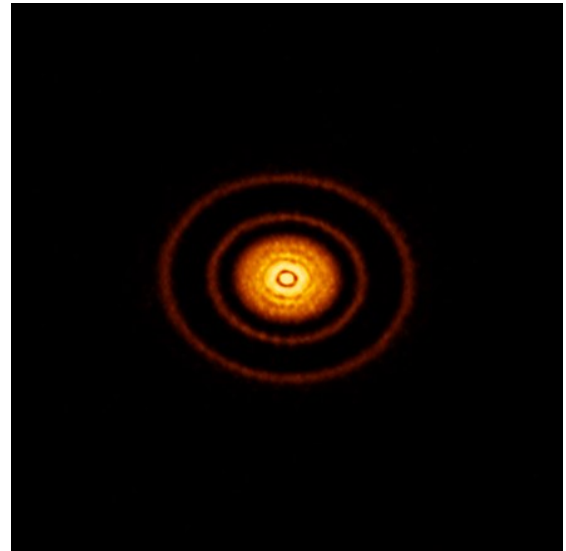
Figure 8: Protoplanetary disk AS 209

Figure 9: Circumstellar disks imaged with ALMA. The submillimetre radiation is sensitive to cold dust that is further away from the central stars not detectable in the infrared anymore. Taken from https://en.wikipedia.org/wiki/Circumstellar_disc.
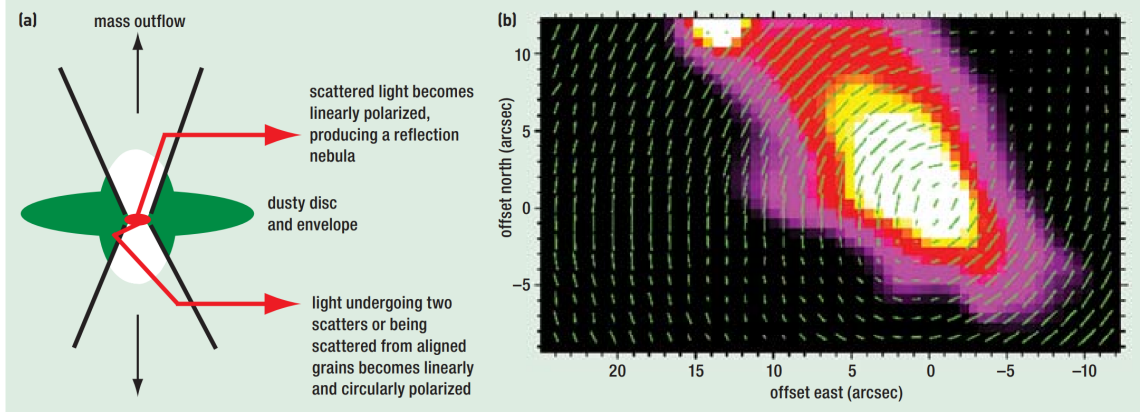
Figure 10: **(a)** Sketch of the dust structure around a young stellar object, taken from [7].
(b) Polarization image at $2.2\,\mu$m of the young stellar object GSS30. The source is at position
(0,0). The line length indicates the polarization degree, the line direction represents the E-vector
of the radiation. 100% polarization corresponds to 6 arcsec. Rotating the image 45° clockswise
would produce the same orientation as in (b). Taken from [7], but originally from [15].

simplest one is the étendue $A\Omega$, which is the product of the aperture of the telescope A and the
solid angle Ω of its field of view, so the portion of the sky it can see with one pointing. Generally,
the étendue is a measure for the amount of energy flowing through an optical system from the
aperture onto the image plane. One can understand this by realizing that the given expression is
proportional to the number of photons gathered by a telescope, given the same reference source
population. This means a telescope with a higher étendue can collect more light and/or see a
bigger portion of the sky. Amateur telescopes with a high étendue often come with an enhanced
capability for wide-field imaging, since it is cheaper to build a telescope with a bigger field of view
than to build one with bigger aperture. Note that A can decrease because of secondary mirrors
or instrumentation in the optical path, and that Ω depends on the chosen image circle, which can
be subject to quality considerations. Moreover, one can formally accomodate the efficiency of the
sensor and the resolution of the system by defining the étendue as $\epsilon = A\eta\Omega/\mathrm{d}\Omega$, where η is the
quantum efficiency of the light detector and $\Omega/\mathrm{d}\Omega$ is the total number of resolved elements in the
field of view [9].

Although the étendue is a helpful metric for amateur astronomers, astronomically inclined photog-
raphers and even optical professionals when constructing single telescope tubi, it does not provide
direct information on the scientific value of a telescope let alone an observatory. This is were
more elaborate metrics come in, which try to estimate the discovery potential of an observatory
by introducing the signal-to-noise ratio (S/N for short) of a source to be discovered. This can be
defined for different types of sources and noise backgrounds and used as a threshold for detection.

The S/N for circular Gaussian source point spread functions (PSF) at the limit of detection when
background noise dominates is

$$\frac{S}{N} \;=\; \sqrt{\frac{F^2 A_{\text{eff}}^2 t_{\text{E}}^2}{4\pi^2 B A_{\text{eff}} t_{\text{E}}} \cdot \int_0^\infty \mathrm{d}r\, \frac{2\pi r}{\sigma^4} e^{-r^2/\sigma^2}} \;=\; \frac{F A_{\text{eff}} t_{\text{E}}}{\sqrt{4\pi\sigma^2 B A_{\text{eff}} t_{\text{E}}}} \tag{4.1}$$

Where is the F the source flux per unit time per unit area, A_{eff} is the aperture effective collect-
ing area, t_{E} the integration time, B the (dominating) sky background in numbers of photons per
unit time, area and unit solid angle of the sky; σ is the width of the Gaussian PSF. The shape
of the PSF is typically determined by atmospheric seeing, optical abberations, the detector or
angular extent of the source. The integration under the square root is the integration over the
two-dimensional source PSF and can be evaluated as a standard integral. Note that eq. 4.1 is not
valid for measurements in the source-noise dominated limit (e.g. transit detection of exoplanets)
or the read-noise dominated limit.

As soon as the S/N can be determined from practically relevant parameters such as the above, it is possible to measure the scientific output of an observatory under the above presumptions as the volume of space in which sources (down to a threshold intrinsic luminosity) can be detected per unit time, which is called the Grasp $\mathcal{G}$. The calculation is based on calculating the maximum distance to a (point) source which is on the threshold of being detectable given parameters of the telescope. For the seeing-limited case, that is the PSF is mainly shaped be atmospheric conditions and the optical resolution of the telescope does not come into play, the grasp is proportional to

$$\mathcal{G} \ \alpha \ \Omega \frac{S}{N}^{-3/2} A_{\text{eff}}^{3/4} \sigma^{-3/2} \frac{t_{\text{E}}^{3/4}}{t_{\text{E}} + t_{\text{D}}} \tag{4.2}$$

Since the grasp is only a metric to compare observatories, it is not necessary to assign a meaningful number to it, so the above proportionality is enough. Note that the seeing-limited case is a good approximation even for relatively small telescopes, as the visible light diffraction limit is 0.7 arcseconds already for a 20 cm-aperture.

For smaller telescopes, which are diffraction dominated, the scaling is different. The PSFs shape only depends on the telescope geometry, which can be translated to the collecting area assuming circularly symmetric apertures, which changes the scaling with A. This is because the background area contributing to the source decreases with A, which compensates for the increase of the background contribution to the source with A. Diffraction-limited case:

$$\mathcal{G} \ \alpha \ \Omega A_{\text{eff}}^{3/2} \frac{t_{\text{E}}^{3/4}}{t_{\text{E}} + t_{\text{D}}} \tag{4.3}$$

It is possible to define additional versions of the grasp that relate to different scenarios, e.g. for the source-noise dominated case and the information-content grasp, which includes Poisson-noise of the sources to describe measurement processes. However, nothing more is needed to understand the considerations behind the plans for the LAST telescope. As a last general comment about the grasp in relation to planning observatories, it can be mentioned that a sky survey with multiple small telescopes (number N) can be executed in two distinct ways. One possibility is to point each telescope to the same field, which results in the grasp scaling like $N^{3/4}$. Alternatively, they can observe different fields, making the grasp scale like N. However, if they run out of sky at some point, the telescopes will need to be pointed to positions they have already observed, which make the scaling of the grasp drop back to $N^{3/4}$.

The comparison of cost-effectiveness of observatories is enabled by the dependence of the grasp on the collecting area. Provided the observatory does not "run out of sky", its grasp scales with the number of telescopes, but the grasp of one individual telescope grows slower than its area. This way, one can attain the grasp of one larger telescope by combining several smaller telescopes. Generally, it is possible to save money this way if larger telescopes are overproportionally more expensive than smaller ones. Although this is mostly true for professional setups, further improvements on cost-effectiveness are possible by using off-the-shelf parts manufactured for amateur astronomers. One key ingredient for this approach is the availability of high-quality CMOS detectors. This is because the detector has to have a high enough resolution for the whole system to become seeing-limited, especially if it is paired with a telescope with a wide field of view, and the needed large-format CMOS detectors with small pixels have become available only recently. The improvement in cost-effectiveness is due to the considerably lower price off CMOS detectors in comparison to CCD detectors, and to the utilization of mass market products concerning the detectors as well as the telescope tubi. This is why the LAST telescope is planned to consist of 48 telescope tubi with dedicated camera sensors.

One challenge for the cost-effectiveness of the smaller telescopes-approach is information processing and storage. Generally, using more telescopes can also lead to storing more images, so this is an issue to be considered, regarding the upfront cost and processing possibilities to lower the load on the information infrastructure.

4.2 Celestron RASA telescopes

The choice for the LAST telescope, and accordingly for the LAST-prototype used in the context of this report, is the 11 inch Rowe-Ackermann-Schmidt-Astrograph manufactured by Celestron (see fig. 11 for an image of the tubus). Being aimed at amateur astrophotographers, it is a very capable instrument with very high ètendue. There is one larger RASA available from Celestron with about double the ètendue, which is optimized for Space Situational Awareness (i.e. tracking satellites and finding debris) and space surveillance in general. It supports even larger camera sensors and has better performance in the infrared. But the 11 inch version is already seeing limited in most observing conditions (assuming that it is paired with a high enough resolution sensor) and it costs less than one fourth of the biggest tubus. So the scaling of grasp vs. financial investment are, as can be concluded from the discussions in section 4 in favor of the smaller tubus, and the improved infrared coverage is not needed for the science case of LAST.

The RASA is a special version of the Schmidt astrograph (or Schmidt telescope) that offers a short focal length, wide field of view and good optical quality across the field of view.
A typical Schmidt camera consists of a spherical primary mirror and a so-called corrector plate. The latter is an aspherical lens (with polynomial curvature, to be more precise), that looks like a glass window covering the opening of the telescope. The spherical mirror makes light that passes through its center of curvature form an equally good image, which yields a wide field of view. However, it is by itself not able to focus all light rays from the same direction to a perfect image. This can be corrected by the already mentioned Schmidt plate, an idea of the Estonian optician Barnadt Schmidt, who also found a way to manufacture the needed corrector plates, which are weakly positive in the center and weakly negative at the edges.
In a Schmidt camera, the image is actually formed inside the tube between the primary mirror and corrector plate. In the last century, there were actually amateur Schmidt telescopes that had a film holder exactly at this place, which had to be curved only slightly because the image in a Schmidt camera is also curved. To make the high-étendue Schmidt design compatible with modern camera sensors, which are rather flat than curved, one needed to design a new telescope. Furthermore, Celestron consultant Dave Rowe wished for a design that had the focal outside the tube, i.e. in front of the Schmidt plate, because it would be very impractical to handle cameras inside the tube. This is handled by the corrector lenses in the middle of the Schmidt plate. The construction details are visible in fig. 12. The first conceptual version had two lenses, but that required a new corrector plate to be designed and manufactured. To be able to use the existing corrector plates from previous generation Schmidt telescopes, the lens group as well as the primary mirror had to be re-worked. The original prototype of the RASA had three lenses made from common glass types, whereas the production version designed by Mark Ackermann has four lenses made from low disperson glass. This yields sharper star images and and improved spectral coverage, actually over the whole visible range. The achieved sharpness over a large spectral range and field of view can be assessed with the help of the matrix spot diagram, see fig. 13. In addition to allowing the camera placement to in front of the sensor, a clear filter can be placed in front of the lens group, which is also done with the LAST prototype.
The RASA has even more special technical details. For once, correcting lenses and the camera are fully supported by the glass structure of the Schmidt plate, which will only break with about 40 kg weigth attached to it. Furthermore, it features a high-precision focusing system, that is necessitated by the narrow depth of focus, which is in turn caused by the fast focal ratio of about f/2. The revised version of the focusing system features a linear ball bearing mounted on a high-precision steel shaft. On the observers side, focusing happens by turning the focusing knob, which moves the primary mirror on the bearing. However, the knob is compatible with focusing motors, so that the telescope can also be focused remotely. This is necessary for a survey instrument, especially if the observatory consists of many RASAs. However, even with the advanced focusing system system it proved to be tricky to focus the telescope by hand during the observations. Another reason for that could be that the computer downloading the images stood in a building, while the telescope was outside, so that two people had to cooperate for focusing. Finally, the RASA is intended to be equipped with a dew shield to keep water vapor from condensing on the optics. This works by attaching a round, tunnel-like object onto the tubus, through which the telescope can look. If there is a source of heat within the dew shield near the tubus, the air near the opening stays warm enough for water vapor not condense. There is a dedicated heat strip available for the RASA, but

in our case, the cooled camera generated enough heat already.

Coming back to the concept of étendue, one can illustrate why the RASA is a prime choice for observatories such as LAST. The 11-inch RASA has an étendue of $0.48\,\mathrm{m^2deg^2}$, making it more capable for survey operation (or quick wide-field imaging in astrophotography) than most other commercially available telescopes of similar dimension, except for the 14-inch RASA with $1.02\,\mathrm{m^2deg^2}$. The full LAST observatory with 48 RASAs would boast an étendue of about $23.04\,\mathrm{m^2deg^2}$, which is already comparable to some the highest-étendue survey telescope currently in operation, like the Oschin-Schmidt camera at ZTF ($56\,\mathrm{m^2deg^2}$) or Pan-STARRS ($60\,\mathrm{m^2deg^2}$). It even surpasses the SDSS telescope, which comes in only at ($6.0\,\mathrm{m^2deg^2}$).

Figure 11: Tubus of the 11 inch RASA. On the front (left image), one can see the corrector lens assembly with the camera mount in the middle of the Schmidt plate. On the back (right image), the focus knob is visible being attached to an orange surface. Right from it is an air outlet for ventilation. Taken from [9].
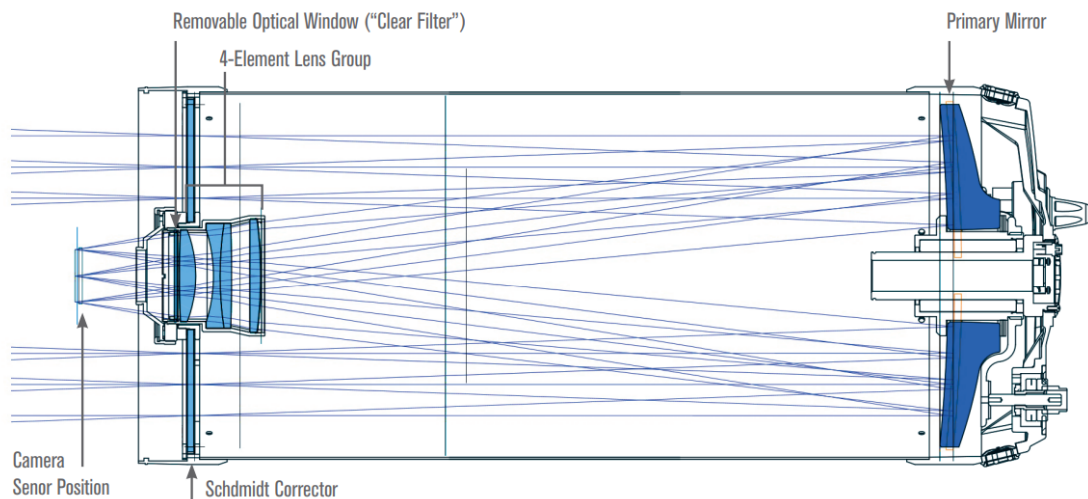
Figure 12: Sketch of the optical design of a RASA. The incoming light rays travel through the Schmidt plate, is reflected at the primary mirror and refocused by the 4-element lens group on the camera sensor position. Taken from [9].
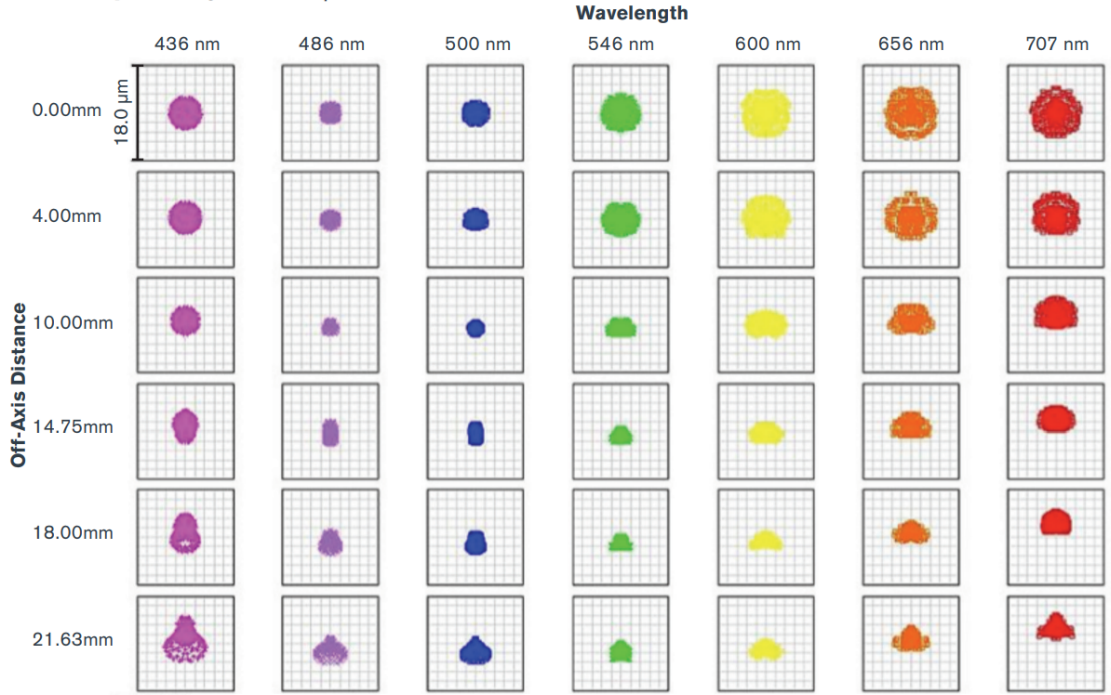
Figure 13: Matrix spot diagram of the 11 inch RASA. This demonstrates that the optical design of the RASA can form tight star images over the whole visible range and its field of view, as the box size is only 18 micrometers. Notice that further from the center, the stars do not become bigger, but rather smaller and deformed. Taken from [9].

5 Theory

In this chapter the theoretical background is given and several methods used in the lab course are outlined. At first, some of the limits to observational astronomy are briefly discussed.

5.1 Limits to observational astronomy

As observational astronomy is done using human-made devices, no ideal measurements can be taken. There are several effects which alter measurements as well as image taking. A brief approach to some of the effect is given in the following.

5.2 Seeing

Given the fact that most observations are done on earth's surface and not in outer space, atmospheric effects alter observations significantly. This is mainly due to turbulence in different atmospheric layers, which become visible as blurring, twinkling or even distortion of celestial light sources. The physical explanation for these appearances are rapid changes in the refractive index of the medium passed along the light path of the measured object. The degree of turbulence and thus the seeing is greatly influenced by weather conditions and temperature gradients in the atmosphere.

To characterize the seeing, the angular diameter of a long-exposure image of a star is measured. The diameter is the full width at half maximum of its optical intensity. The angular diameter is commonly specified at 500 nm wavelength. Excellent seeing is considered at a seeing disk smaller than 0.4 arcseconds. These conditions are normally found at obervatories at high altitudes.

5.2.1 Diffraction

Independent of atmospheric effects, telescopes are also limited by diffraction. The effect of diffraction spikes is reasoned due to the support vanes, a non-circular aperture, segmented mirrors or dirty optics. Furthermore, the image of a point source is an extended pattern of intensity distribution. This is due to interference effects of the light cone. This is called light-diffraction. The diffraction pattern in the plane of focus is inversely proportional to the telescope's relative aperture $\frac{1}{F}$. By this the radius of the first minimum, the airy disc, can be calculated by $r_{\text{Airy}} = 1.22\lambda F$. F is the focal ratio given by $F = \frac{f}{D}$ with f the focal length and D the diameter of the telescope. To estimate the influence of diffraction on image quality the angular size of the diffraction pattern is used. The angular size is given by $\alpha_{AD} = 1.22\frac{\lambda}{D}$ in radians. By this formula the resolution and maximum magnification of a telescope is directly limited. [2]

5.2.2 Methods to overcome these difficulties

Doing science, it is important to minimize uncertainties of measurements and to account for those uncertainties which cannot be minimized.

At first, the seeing can not be influenced by the physicist. Still, to get the least influence of bad seeing, the observation site can be chosen carefully, as well as the date and time of observation. The less atmospheric matter there is between observer and celestial object, the less turbulence can alter the seeing. Therefore, it is desirable to locate the observation site on the highest altitude possible. Furthermore, as the seeing is greatly dependent on atmospheric effects and weather conditions, the date of observation can be chosen to be one with good seeing, using weather forecasts and choosing the season with the most stable weather forecast for the respective location.

In the case of this lab course, the observation site was set to the observation site at the Ruhr-Universität Bochum next to the botanical garden, mainly due to logistic reasons. The university is located on a hill with mediocre light pollution. Moreover the weather forecast was carefully analyzed before observations were scheduled by the lab course instructor.

To minimize diffraction effects, it is useful to know the capabilities of the used telescope and, if possible, constructing it in a diffraction-reducing manner. This can be done by analyzing the most useful support vane setup for the purpose of the telescope using a circular aperture and no segmented mirror, but this is always dependent of the purpose of the telescope, such as mobility, material cost and other aspects. Furthermore, it is important to take care of the optics, to reduce

diffraction spikes due to dirt, hair, grease etc.

To minimize these and other effects, the data taking in observational astronomy is normally done by doing several steps before the actual observation as well as data reduction. These steps are described in chapter 5.4.

5.3 Polarization Degree and Angle

Measuring polarization degree and angle is often done using the **Stokes-Parameters** I, Q, U and V. This procedure was introduced by George Gabriel Stokes in 1852. The main aspect of using the Stokes parameters is that the polarization information of a given source can be easily determined by measuring the radiated power of the source after passing through several polarization filters. The Stokes parameters are defined as follows:

$$Q = \frac{I_0 - I_{90}}{I_0 + I_{90}} \tag{5.1}$$

$$U = \frac{I_{45} - I_{135}}{I_{45} + I_{135}} \tag{5.2}$$

With I_{α° the intensity after passing through horizontal ($0°$), vertical ($90°$), $45°$ and $135°$ rotated polarization filter. Note that one needs four intensity measurements respectively filter positions only because the polarization angle is not known *a priori*. If it would be known, one could simply position the filter once parallel and once orthogonal to it to obtain the polarization degree.

In this lab course, only linear polarized light will be of interest. This leads to some simplification. The Stokes parameter then yield for the linear polarized light the polarization degree PD as follows.

$$PD = \sqrt{Q^2 + U^2} \tag{5.3}$$

The polarization angle is defined as follows.

$$PA = \tan^{-1}\left(\frac{U}{Q}\right) \tag{5.4}$$

The uncertainties on these values are calculated using Gaussian error propagation as follows.

$$\sigma_Q = \frac{2}{(I_0 + I_{90})^2} \cdot \sqrt{I_{90}^2(\sigma_{I_0})^2 + I_0^2(\sigma_{I_{90}})^2} \tag{5.5}$$

$$\sigma_U = \frac{2}{(I_{45} + I_{135})^2} \cdot \sqrt{I_{135}^2(\sigma_{I_{45}})^2 + I_{45}^2(\sigma_{I_{135}})^2} \tag{5.6}$$

$$\sigma_{PD} = \sqrt{\frac{Q^2 \cdot \sigma_Q^2 + U^2 \cdot \sigma_U^2}{Q^2 + U^2}} \tag{5.7}$$

$$\sigma_{PA} = \sqrt{\frac{Q^2 \cdot \Delta U^2 + U^2 \cdot \Delta Q^2}{(U^2 + Q^2)^2}} \tag{5.8}$$

The information on polarization angle and degree can then be used for further analysis, as described before. The main aspect of this lab course will be to determine the polarization degree and angle of different, already known sources to collect calibration data for a new telescope setup.

5.4 Data Analysis and Image reduction

To measure the polarization of the light emitted by a celestial object, it is favorable to use a setup with a telescope with an integrated camera system, in this case an CCD in front of the telescope tube. As taking a simple picture of the star is not sufficient for a meaningful analysis, it is important to do some calibration before actually observing. These calibration consists of three different measurements taken before the actual observation starts. These are known as *darkframes*, *flatfields* and *biasframes*.

5.4.1 Biasframe

As the measurements are done using an electronical operating camera system, it is probable that the system is not perfect, resulting in a current between the time of exposure and the signal processing, which alters the charge on each pixel even with no exposure. This current can be described by statistical properties, and is always roughly the same for one setup. To approach this problem, the bias frame is taken. This frame is supposed to measure aberrations in the signal of each pixel from the actual measured amount of photons. To do so, the shutter is covered, so that no external light can reach the sensor. Taking a measurement with the shortest exposure time possible, on receives a *picture* containing only the statistical current measured. As the current is varying statistically, it is reasonable to take multiple biased frames and use a measure of central tendency of each pixel in the measured biased frames. This also accounts for the possibility of cosmic particles passing through a pixel, leading to an unusual high charge on one specific pixel. It is important to use a method of mean-calculation like the median, as the arithmetic mean does not eliminate extreme aberrations, but just weakens them. The calculated mean bias is called the **Master Bias**. To account for the bias, the Master bias is just substracted from the images taken during the observing run.

5.4.2 Darkframe

The next step in calibration is done using the dark frame. During exposure, incoming photons hitting the pixels lead to electron emission. Ideally, exactly one electron is emitted for each incoming photon. Additionally, as the atoms in the sensor / chip are moving due to temperature, further electrons are emitted in each pixel, even with the shutter closed. This additional current is called dark current, as it is also present with no light falling onto the sensor. The dark current is individual for each pixel and strongly temperature dependent. Pixels with an extraordinary high dark current are called *hot pixels*. To account for this dark current, the dark frame is taken. This dark frame accounts for the emission of free electrons in each pixel per time unit. To do so, the shutter is closed and the sensor is set to measure for the longest possible time. The longer the exposure time, the better the statistical measurement for the dark current of each pixel. Still, if the exposure is too long, some pixels may reach their full well capacity, resulting in electrons wandering to neighbouring pixels, altering the calibration again. It is important to take the dark frame at the same temperature, as the observation later is exercised (high temperature dependence). Again, taking several dark frames also reduces statistical uncertainties. To obtain the **Master Dark**, the averaged dark frame is subtracted by the Master Bias and divided by the exposure time to receive the dark current per time unit.

To account for the dark, the picture taken in the observation later on is corrected for the bias first and then subtracted by the Master Dark times the exposure time of the picture taken in the observation.

5.4.3 Flatfield

The third step in calibration is the flatfield. The flatfield accounts for imaging errors due to the optics. Using the flatfield, errors like vignetting or edge light falloff can be reduced. To take the flatfield, the telescope is pointed at an uniform surface, like an evenly lit part of the sky just after sunset. Due to the optical errors, the intensity measured will not be uniform, unlike expected when pointing at an uniform surface. In our observations, the sky was taken as an uniform surface right after sunset. Again, taking several images is advantageous. It is important to correct each flatframe for bias and dark before averaging them to the **Masterflat**. To account for the Masterflat in the observation later on, the bias and dark corrected image is divided by the Masterflat.

5.4.4 Data analysis

On the observation site, after taking bias, dark and flat frame, the object of interest is observed. Again, it can be advantageous to take multiple images and **stacking** them later. This procedure is not explained in detail here, as in this analysis no images are stacked. Instead, the images are simply averaged and the result is fitted to a Gaussian PSF to obtain the magnitude of the object

of interest. Here, the magnitude is calculated four times, as the polarization filter is rotated 45°
into four positions. By doing so, the polarization degree and angle of the source can be calculated
as described in section 5.3. For further analysis, the magnitude is converted to values of intensity
with the following relation:

$$I_x = 10^{-\frac{Mag}{2.5}} \qquad (5.9)$$

The uncertainty of the intensitiy is then given by the following relation:

$$I_{x,err} = I_x - 10^{-\frac{(Mag+Mag_{err})}{2.5}} \qquad (5.10)$$

6 Setup and the LAST-prototype

The observations were conducted with the LAST-prototype at the Astronomical Institute at the
Ruhr-Universität Bochum, which consists of an 11 inch Rowe-Ackermann-Schmidt Astrograph
(RASA for short) manufactured by Celestron, mounted on an equatorial mount manufactured by
Losmandy and placed on a tripod with wheels. The technical details of this telescope are discussed
in sec. 4.2 The telescope is equipped with a remotely controlled polarization filter and a red filter
of the same spectral response as is going to be used for the LAST observatory. This way, one
ensures accurate photometric measurements that are not influenced by emission lines from the sky.

7 Observation procedure

7.1 Parking the telescope

Roughly an hour before twilight, the telescope is taken out from the observer's bungalow and carried
to the platform, which lacked a dome during the time of observation. There, the mount, the camera
and the filter mount are connected to a computer which is placed next to the telescope. However,
the computer is remotely controlled via an Ethernet-hub from inside the observer's bungalow. In
addition, the camera cooler is switched on and set to a certain sensor temperature.

7.2 Taking the calibration images

To save time, the flatfields are taken first, because they are images of a uniform part of the sky
during twilight, whereas the dark and bias frames can be taken at any time, provided that the
sensor has reached its target temperature. For that, the telescope is pointed towards a suitable
portion of the sky and several short exposures are taken. However, one needs to wait until the
sky is dark enough so that the photon counts of the CCD sensor are reliable. In practice, that
means that the brightest parts of the image do not contain more than around 40,000 photons per
pixel. The electron wells in the sensor can deal with slightly more than 60,000 photons, and it is
advisable to have a comfortable margin up to this limit to ensure sharp star images. This criterion
also applies when imaging the sources, where the exposure time is adjusted to match it. For testing
observations such as this one, only the source to be observed was considered. Of course, this will
be handled differently in later survey operation, where the sources of interest are many and appear
unexpectedly.

7.3 Aligning the mount

As the telescope is mounted on an equatorial mount, it has to be aligned with the axis of the
sky. This is done in sufficient darkness so that the pole star camera can image Polaris and several
surrounding stars. The pole star camera is placed at a specially designed site on the mount, so
that its field of view is aligned with the axis of the equatorial mount. It does not have a dedicated
telescope, only a small telephoto lens comparable in aperture with a smartphone camera.
It is operated with a dedicated software running on a dedicated laptop, so that one can sit next to
the telescope while aligning the mount. The software shows video output from the pole star camera
overlaid with a mask of circles at the relative positions of several bright stars around Polaris. The
task is then to position the telescope mount (and rotate the star mask in software) in such a way

that all circles have a star inside. This is done by adjusting certain precision screws on the mount, not by steering the motors. If the telescope is now rotated around its hour axis (this time with the motors), all of the stars should move in circles around the north pole of the sky. It is, however, enough to check for one, since stars are fixed.

7.4 Finding the target

If the foregoing steps are successfully completed, the observation can start. Firstly, one needs to roughly tell the telescope mount where it looks, which is usually towards Polaris. This indication does not need to be too precise, because the field of view is so wide and further fine tuning with an accuracy of about 10 pixels is done manually once a source is found. Notice that steering the telescope "manually" still means via the control software. Furthermore, the geographical coordinates as well as the elevation have to entered into the mount control software, so that the directions of mechanical movement of the mount can be translated to directions on the sky. Often, the mount can move to the position of the desired source by itself, following its inbuilt catalog. Otherwise, the sources have to be targeted via their coordinates. During some observations, the mount showed totally erratic behaviour, pointing the telescopes towards the earth when it was obvious that it should be pointing towards a constellation well visible in the sky. In such cases, one can try to find a well visible star near the source of interest by spotting its constellation and pointing the telescope there manually. However, this is really difficult with the setup that was available here, since the RASA was not equipped with a guiding scope. This means one person had kneel down behind the telescope, estimate were it was looking (which is the difficult part) and tell the operator in the bungalow in which direction to move the mount.

When the field is found, one uses a finding chart to identify the source, which is usually not a prominent star. The star charts are based on different sky surveys and can be viewed on a website operated by the NASA. They are calculated according to input specifications, such as sky coordinates at the center, field of view, location and elevation (they determine the orientation of the sky map), which range of magnitude to include for the sources and various options for colouring and presentation. Actually finding the source is an exercise that requires experience in recognizing star patterns. Mostly, it is done within a few minutes by a more experienced observer. Newbies like the authors of this manual took slightly longer. In rare cases, the sources could not be found even by experienced observers, leaving the question open if the telescope was actually pointed to the patch of the sky that the star chart depicted.

7.5 Images for polarization measurement

Once the source is found, it was moved to an intended position on the sensor, steering the mount with the remote control software. For the observations that form the basis of this protocol, this was always the center of the image sensor, about the same place where the optical axis intersects with it. During further observations, other points in the image plane have been chosen to calibrate the polarization measurements with LAST across its field of view.

Then, the measurement procedure is started by taking at least four (sometimes more) images of the source with the polarization filter in different angular positions. The remote control software of the camera is set so that it takes and downloads the images one after the other automatically, leaving short breaks on the order of 30 seconds in between. Within these breaks, the filter must be rotated "manually" using the remote control software of the filter mount by the operator. More concretely, one has to click on a software button to turn the filter by 45 degrees. If the filter position is not within a certain level of tolerance, which can be assessed because the filter mount has a position sensor, the filter is rotated again, but this time to a preset position angle.

8 Measurements and discussion

In this section, the measurement of different polarization parameters is outlined and the calculated polarization degrees and angles are presented. The measurements were taken in two nights of observation with changing observers and different conditions. In the first night following Oct 23rd, 2021, Leonard observed the three sources on top of the list, with two sources being observed twice. The other three were observed by Patrick. Both Patrick and Leonard participated at additional observing runs of the LAST prototype.

At first, the steps described in section 7 were done and the telescope is aimed at different sources of interest. Then, the source is exposed 4 times. Each exposure, the polarization filter inside the telescope setup is turned 45°. The data is then corrected and reduced as described in section 5.4. This yields a fit for the magnitude of the object with the respective filter setting. Using the magnitude, the stokes parameters, the polarization degree and the polarization angle can be calculated as described in section 5.3. Table 1 shows the measured Stokes parameters and table 2 the calculated polarization degree and angle for β Cassiopeiae, a Delta Scuti variable star, BL Lacertae, the prototype blazar and the stars HD25443, HD191195 and HD25443.

Table 1: Stokes parameters for all sources observed for this protocol

Source	U	Q
BL Lac	-0.095267 ± 0.006151	0.085355 ± 0.006257
BL Lac 2	-0.0381123 ± 0.0058962	0.0985520 ± 0.00628911
HD191195	0.00483539 ± 0.001107	0.0045130 ± 0.001107
HD204827	-0.055022 ± 0.0013314	0.0143671 ± 0.00130226
HD204827, again	-0.023758 ± 0.00136689	0.0412848 ± 0.0013332
BL Lac 3	0.0757 ± 0.01081	-0.02436 ± 0.01027
β Cas	-0.00755 ± 0.00094	-0.00461 ± 0.00098
HD25443	-0.04942 ± 0.00094	0.00368 ± 0.00091

Table 2: Polarization degree and polarization angle for all measured sources including two references from literature (marked by *, see [13] and [14]). The topmost three have been observed in the first night by Leonard, the last three above the references in another night by Patrick.

Source	PD[%] (relative deviation)	PA [rad]
BL Lac	12.8 ± 0.62 (4.8%)	-0.84 ± 0.048
BL Lac 2	10.6 ± 0.62 (5.9%)	-0.34 ± 0.056
HD191195	0.66 ± 0.11 (16.7%)	0.82 ± 0.167
HD204827	5.79 ± 0.13 (2.3%)	-1.31 ± 0.022
HD204827, again	4.76 ± 0.13 (2.8%)	-0.52 ± 0.028
BL Lac 3	7.95 ± 1.01 (13.5%)	-1.26 ± 0.13
β Cas	0.89 ± 0.095 (10.8%)	1.02 ± 0.101
HD25443	4.96 ± 0.094 (1.9%)	-1.50 ± 0.018
HD25443 R-band reference *	4.73 ± 0.045 (0.95%)	2.333 ± 0.0049
HD204827 R-band reference *	4.89 ± 0.029 (0.59%)	1.03 ± 0.030

It has to be noted that we tried to ensure correct computation of both the polarization degree and the polarization angle with their respective uncertainties by first writing two separate Python scripts and finally another one (see section 8) and analysing all of our data with all of them. With PD and PA themselves, we succeeded and are therefore fairly certain that the values are the correct result of our measurements. The same holds true for the uncertainties, however it must be noted that the uncertainties on PD and PA of BL Lac, BL Lac 2, HD191119 and both measurements of HD204827 were different when calculated with Patrick's script than with either of Leonard's scripts, which were developed independently. The uncertainties for BL Lac 3, β Cas and HD25443 were the always same, however, so we suspect an error in the handling of the input data rather

than in the computation. This is further indicated by the finding that the dubious uncertainties calculated with Patrick's script were also strangely high, for instance reaching to 80% for the PD of BL Lac. In summary, the values we present are either consistent across all scripts or across Leonard's two scripts.

In the two last columns of table 2, two reference values are included, more precisely PD and PA for the stars HD25443 and HD204827. Our measurement of PD in HD25443 is off by about 0.22% while our 1σ-confidence interval is only 0.094%. This is not a good result by itself, since we can assume the reference value measured about 40 years ago to be still correct today and we are off by more than 2σ. However, considering many more measurements with the LAST prototype, such values might reflect systematical errors and can therefore be used for calibration.

Our more compatible measurement of PD of HD204827 is exactly one standard deviation (ours, not that of the reference) apart from the reference value for PD. This alone could be considered a success, but our first measurement of HD204827 stands in strong conflict, differing by 1.03% although our measurement error is only at 0.13%. An obvious possible reason would be that the intensities might have been put in a wrong relation towards one another during the calculation of the Stokes parameters. This could happen because the filter was turned to different positions, namely 180°, 225°, 270° and 315°, in the second observation. But this has been double- and triple-checked, so we assume that the mistake is not within the calculation or the re-assignment of variables in the script. We also exchanged the values of the intensities in a way that would neutralize a possible mix-up of I_0 and I_{45} or I_{90} and I_{135} in the calculation of U and Q, but that made the difference dramatically worse. In summary, this difference between two measured PD's of the same star in one night remains mysterious. At least the uncertainties are exactly at the same absolute level, which makes sense.

Considering the blazar, it appears as the object with the highest polarization degree in our list. This is not a surprise, since it is known that the PD of BL Lac in the V-Band can change from around 5% to 25% and even by 10% within a few weeks [12]. This could also explain the difference in PD between our two observing nights, which is about 3% and substantially bigger than the uncertainties on that value.

What is not so easy to explain is the difference in PD of both observations in the first night, which is almost exactly two standard deviations. Lacking clear statistics, i.e., more observations during the same night, one cannot even say how much of a problem this is. To get an estimate on this issue, we simulated $2 * 10^6$ measurement values from a random normal distribution, separated in two distinct datasets. Then, we drew 10^5 randomly chosen pairs, one member from each dataset, and calculated the difference. It turned out that slightly more than 32% of them were between 1σ and 2σ apart, slightly more than 12% between 2σ and 3σ and slightly more than 3% more than 3σ. That means that a pair of measurements with difference as extreme or more extreme than the difference of our blazar PDs should regularly occur in about 15%-16% of the cases. This suggests that one does not need to worry about a 2σ difference if it just happens for two single measurements, so this discrepancy is acceptable for now.

It has to be noted, though, that the uncertainties on PD of BL Lac seem to have risen by about a factor of two from the first to the second night of observation, which might be attributable observing conditions, although we cannot confirm that. Moreover, the brightness of the sources (given the applied exposure) seems to play a role in creating to uncertainties, since the measured intensities (not shown in this protocol) were about 10 to 40 times higher for the stars. It therefore fits that the absolute uncertainties on PD of BL Lac are considerably bigger in each respective night than those for the stars. One may remember that the uncertainties on PD scale with the square root of the square of the intensities scaled by some square of an uncertainty, but also with the square of the sum of the intensities in the prefactor.

Trying to examine another possible reason for the different uncertainties of the final polarization degrees, one can take a closer look. It is clear that the uncertainties on PD essentially derive from those of the intensities respectively the magnitudes of the sources which are measured from the images with the polarization filter in different orientations. That happens by fitting a Gaussian point spread function to the source, and the accuracy of the inferred amplitude essentially depends on the noise level in the image in relation to the source strength. More background noise in the

sky right next to the source will lead to higher uncertainties for the intensities and accordingly for the polarization degree. That means one can explain differences between nights simply by the observing conditions, at least tendencially. For example, in a night that is slightly more hazy or that has more straylight from the moon, the sky will be brighter, the background noise levels higher and the measurements more uncertain. Similarly, a source which is positioned further away from zenith is observed through a longer optical path through the atmosphere, which should also add background noise and therefore uncertainties.

However, the visibility plot for Leonards sources (on Oct 23rd, 2021 in Bochum) indicates that the previous reasons cannot have caused the difference in uncertainty of the polarization measurements between the blazar and the stars within one night. In fact, the height of the three sources in the sky at the beginning of the night was similar, with BL Lac and HD204827 being almost the same. The same argument holds for the moon distance. At 22:20 local time, it was 90.2 degrees for HD191195, 77.5 degrees for HD204827 and 77.7 degrees for BL Lac (calculated as part of the visibility plot in fig. 14). This means that there was not more moonlight in the background of BL Lac compared to one of the stars which have a substantially lower uncertainty on the polarisation, while the possible difference in contamination with moonlight between the two stars does not lead to a difference in measurement uncertainties. This indicates that the difference in polarization between the stars and the BL Lac was indeed probably due to difference in intrinsic brightness. Although we cannot exclude temporary differences in the cloud cover, these are more improbable, since the difference is there in each night across all observations.

We have also included the polarization angles into this report, eventhough we cannot comment on them, since we have no means to put them in relation to any coordinate system and reference orientation. Anyway the telescope changed its orientation when looking at different sources, and we have no reason to believe that the rotating filter holder automatically corrected for that. So what is I_0 for one source might be $I_{27.93}$, $I_{263.09}$ or anything else for another one, which makes the polarization degrees incomparable even among the set of our observations, let alone the reference observations of HD25443 and HD204827. Within the final LAST observatory, there will of course be the possibility to combine the position of the filter holder with information about the orientation of the telescope and/or the camera and the sky, so that polarization angles can be measured properly.

To sum up, one might say that BL Lac is an interesting source since it changes its polarization degree due to internal dynamics. The stars that we observed, are, however, standard stars and were selected so that they are constant in polarization and can be used for calibration purposes, e.g., for the LAST prototype. Comparing our measurements to the references mentioned, it is quite reassuring that the uncertainties on PD of the stars are in general quite low and only by a factor of about 2 to 4 higher than those of the references. The only really problematic measurement is the first one of HD204827, which fits neither to our second one nor to the reference, lacking an explanation. The differences in PD for BL Lac during the first night are more than obvious, but not a problem, since a disagreement like this or worse is bound to happen in more than about 1/6 of the cases, just because of statistical uncertainties.

Moreover, the differences in the uncertainties between the blazar, which is known to change its PD within weeks, and the stars can probably be explained by the intrinsic difference in brightness of the sources, since the observing conditions are likely to have been about the same. In addition, the differences in uncertainties of PD when comparing the stars from one night to the stars of the other are so small (e.g., 0.13 vs. 0.094) that they need no explanation.
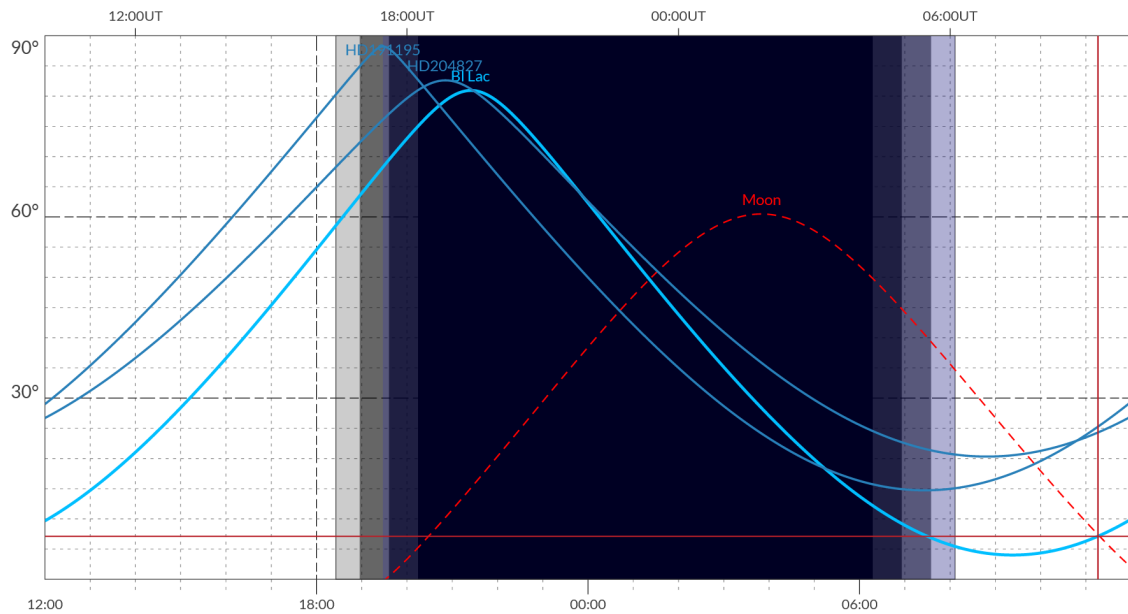
Figure 14: Visibility plots for BL Lac, HD191195 and HD 204827 for Oct 23rd, 2021 in at the very location of the observatory, that is 51° 26' 30.76" N 07° 15' 45.94" E at 150 m altitude. The curve of HD191195 peaks the highest while the curve of BL Lac is in a lighter, bolder blue. Produced with `https://airmass.org`.

References

[1] *Polarisation (Astronomie)*, Last Access 23.02.2022
`https://de.frwiki.wiki/wiki/Polarisation_(astronomie)`

[2] *Diffraction*, Last Access 27.11.2022
`https://www.telescope-optics.net/diffraction.htm`

[3] *An example CMOS sensor*, Last Access 09.02.2023
`https://www.edmundoptics.de/p/Allied-Vision-Alvium-1800-U-500m-125-50MP-Right-Angle-USB-31-Monochrome-42349?gclid=CjwKCAiA0JKfBhBIEiwAPhZXDy2Ah5j5ScdhP8PXO668-F_0p89LzzEYv1tFtIPr5LfLXXSMlsn0txoCcOAQAvD_BwE#`

[4] *CMOS CCS Comparison*, Last Access 09.02.2023
`https://www.wileyindustrynews.com/news/cmos-vs-ccd-technologien#:~:text=Ein%20grunds%C3%A4tzlicher%20Unterschied%20dabei%20ist,eine%20Rolling%2DShutter%2DFunktion.`

[5] Hohmann, *Quantum efficiency*, Last Access 09.02.2023
`https://astrofotografie.hohmann-edv.de/grundlagen/glossar.php?Stichwort=Quanteneffizienz`

[6] E.O. Ofek and S. Ben-Ami, *Seeing limited Imgaging Sky Surveys - Small versus large Telescopes* (2020)
`https://ui.adsabs.harvard.edu/abs/2020PASP..132l5004O`

[7] James Hough, *Polarimetry: a powerful diagnostic tool in astronomy* (2006)
Published in *Astronomy & Geophysics volume* 47

[8] Sascha Trippe, *Polarization and Polarimetry: A Review* (2014)
Journal of the Korean Astronomical Society Volume 47, pages 15 − 39

[9] Richard Berry and the Celestron Engineering team, *Big! Fast! Wide! Sharp! The Story of the Rowe-Ackermann Schmidt Astrograph* (2020)

[10] *Optical Tube Assembly*, Last Access 23.02.2023
`https://www.celestron.com/products/11-rowe-ackermann-schmidt-astrograph-rasa-11-v2-optical-tube-assemb`

[11] Zuckerman, Ben, *Dusty Circumstellar Disks.* in Encyclopedia of Astronomy and Astrophysics, pg. 638-644 Institute of Physics Publishing, Bristol and Philadelphia; Nature Publishing Group, London, New York and Tokyo (2001)

[12] Haritma Gaur et al., *Multi-Band Intra-Night Optical Variability of BL Lacertae* in Galaxies, Vol. 5, no. 4, pg. 94 (2017)

[13] J. C. Hsu and M. Breger, *On standard polarized stars* in The Astrophysical Journal, v. 262, p. 732-739 (1982)

[14] D. P. Clemens and S. Tapia, *Toward Selection of Intermediate Magnitude Polarization Standards* in Publications of the Astronomical Society of the Pacific, v.102, p.179 (1990)

[15] Antonio Chrysostomou, *Polarimetry of young stellar objects - I. Linear polarization of GSS 30* in Monthly Notices of the Royal Astronomical Society, v. 278 p. 449 (1996)

.1   Leonards code

```python
import numpy as np

def calc_u(I45=1.0, I135=1.0, sigma_I45=0.0, sigma_I135=0.0):
    U = (I45 - I135) / (I45 + I135)
    sigma_U = 2 / (I45 + I135)**2 * np.sqrt(I135**2 *sigma_I45**2 + I45**2 *sigma_I135**2)
    return U, sigma_U


def calc_q(I0=1.0, I90=1.0, sigma_I0=0.0, sigma_I90=0.0):
    Q = (I0 - I90) / (I0 + I90)
    sigma_Q = 2 / (I0 + I90)**2 * np.sqrt(I90**2 *sigma_I0**2 + I0**2 *sigma_I90**2)
    return Q, sigma_Q


def calc_pd(Q=1.0, U=1.0, sigma_Q=0.0, sigma_U=0.0):
    pd = np.sqrt(Q**2 + U**2)
    sigma_pd = np.sqrt(( Q**2 *sigma_Q**2 + U**2 *sigma_U**2) /(Q**2 + U**2))
    return pd, sigma_pd


def pol_angle(U=0.0, Q=0.0, sigma_U=0.0, sigma_Q=0.0):
    pa = np.arctan(U/Q)
    sigma_pa = np.sqrt( (Q /(Q**2 + U**2) * sigma_U)**2 + (Q /(Q**2 + U**2) * sigma_Q)**2 )
    pa_deg = pa /(2 *np.pi) *360
    sigma_pa_deg = sigma_pa /(2 *np.pi) *360
    return pa, sigma_pa, pa_deg, sigma_pa_deg


def mag2int(mag=0.0, mag_ref=1.0, I_ref=1.0, sigma_mag=0.0):
    I = I_ref * 10**((mag_ref - mag) /2.5)
    sigma_I = np.abs( np.log(10) *0.4 *10**(mag_ref *0.4) * I_ref * 10**(-mag *0.4) *sigma_mag)
    return I, sigma_I

bl_lac_1 = {"name": "BL Lac again", "p000": 13.4523, "d_p000": 0.0087,
            "p045": 13.5731, "d_p045": 0.0096,
            "p090": 13.6670, "d_p090": 0.0107,
            "p135": 13.4903, "d_p135": 0.0085,
            }

bl_lac = {"name": "BL Lac", "p000": 13.4700, "d_p000": 0.0089,
            "p045": 13.6437, "d_p045": 0.0107,
            "p090": 13.6558, "d_p090": 0.0104,
            "p135": 13.4362, "d_p135": 0.0082,
            }

hd_191195 = {"name": "HD 191195", "p000": 11.1814, "d_p000": 0.0017,
            "p045": 11.1772, "d_p045": 0.0017,
            "p090": 11.1912, "d_p090": 0.0017,
            "p135": 11.1877, "d_p135": 0.0017,
            }

hd_204827 = {"name": "HD 204827", "p000": 11.5464, "d_p000": 0.0020,
            "p045": 11.6418, "d_p045": 0.0021,
            "p090": 11.5776, "d_p090": 0.0020,
            "p135": 11.5222, "d_p135": 0.0020,
            "p180": 11.5799, "d_p180": 0.0020,
            "p225": 11.6445, "d_p225": 0.0021,
            "p270": 11.6696, "d_p270": 0.0021,
            "p315": 11.5929, "d_p315": 0.0021,
            }
```

```python
my_star = hd_204827
I0, sigma_I0 = mag2int(mag=my_star["p000"], sigma_mag=my_star["d_p000"])
I45, sigma_I45 = mag2int(mag=my_star["p045"], sigma_mag=my_star["d_p045"])
I90, sigma_I90 = mag2int(mag=my_star["p090"], sigma_mag=my_star["d_p090"])
I135, sigma_I135 = mag2int(mag=my_star["p135"], sigma_mag=my_star["d_p135"])

U, sigma_U = calc_u(I45=I45, I135=I135, sigma_I45=sigma_I45, sigma_I135=sigma_I135)
Q, sigma_Q = calc_q(I0=I0, I90=I90, sigma_I0=sigma_I0, sigma_I90=sigma_I90)
pd, sigma_pd = calc_pd(Q=Q, U=U, sigma_Q=Q, sigma_U=sigma_U)
pa, sigma_pa, pa_deg, sigma_pa_deg = pol_angle(Q=Q, U=U, sigma_Q=Q, sigma_U=sigma_U)

print("\nSource: ", my_star["name"])
print("I0 = ", I0, " +- ", sigma_I0)
print("I45 = ", I45, " +- ", sigma_I45)
print("I90 = ", I90, " +- ", sigma_I90)
print("I135 = ", I0, " +- ", sigma_I135)
print("U = ", U, " +- ", sigma_U)
print("Q = ", Q, " +- ", sigma_Q)
print("polarization degree = ", pd, " +- ", sigma_pd, " +- ", sigma_pd/pd*100, " %")
print("polarization angle = ", pa, " +- ", sigma_pa, " +- ", sigma_pa/pa*100, " %")
print("polarization angle = ", pa_deg, " +- ",
sigma_pa_deg, " +- ", sigma_pa_deg/pa_deg*100, " %")
```

.2   Leonards second code

```python
import numpy as np

# FROM LEONARDS OBSERVATION
bl_lac = {"name": "BL Lac", "p000": 13.4700, "d_p000": 0.0089,
          "p045": 13.6437, "d_p045": 0.0107,
          "p090": 13.6558, "d_p090": 0.0104,
          "p135": 13.4362, "d_p135": 0.0082,
          }


bl_lac_1 = {"name": "BL Lac again", "p000": 13.4523, "d_p000": 0.0087,
          "p045": 13.5731, "d_p045": 0.0096,
          "p090": 13.6670, "d_p090": 0.0107,
          "p135": 13.4903, "d_p135": 0.0085,
          }



hd_191195 = {"name": "HD 191195", "p000": 11.1814, "d_p000": 0.0017,
          "p045": 11.1772, "d_p045": 0.0017,
          "p090": 11.1912, "d_p090": 0.0017,
          "p135": 11.1877, "d_p135": 0.0017,
          }


hd_204827 = {"name": "HD 204827", "p000": 11.5464, "d_p000": 0.0020,
          "p045": 11.6418, "d_p045": 0.0021,
          "p090": 11.5776, "d_p090": 0.0020,
          "p135": 11.5222, "d_p135": 0.0020,
          "p180": 11.5799, "d_p180": 0.0020,
          "p225": 11.6445, "d_p225": 0.0021,
          "p270": 11.6696, "d_p270": 0.0021,
          "p315": 11.5929, "d_p315": 0.0021,
          }
```

```python
# renaming some data to be processed in a loop
hd_204827_2 = {"name": "HD 204827 again", "p000": 11.5799, "d_p000": 0.0020,
               "p045": 11.6445, "d_p045": 0.0021,
               "p090": 11.6696, "d_p090": 0.0021,
               "p135": 11.5929, "d_p135": 0.0021,
               }


# FROM PATRICKS OBSERVATION
bl_lac_p = {"name": "Bl Lac", "p000": 14.3198, "d_p000": 0.0161,
            "p045": 14.2275, "d_p045": 0.016,
            "p090": 14.2669, "d_p090": 0.0157,
            "p135": 14.3922, "d_p135": 0.0176,
            }


cas_p = {"name": "beta Cas", "p000": 10.9186, "d_p000": 0.0015,
         "p045": 10.9026, "d_p045": 0.0015,
         "p090": 10.9086, "d_p090": 0.0015,
         "p135": 10.8862, "d_p135":  0.0014,
         }


hd_25443 = {"name": "HD 25443", "p000": 10.862, "d_p000": 0.0014,
            "p045": 10.9275, "d_p045": 0.0015,
            "p090": 10.87, "d_p090": 0.0014,
            "p135": 10.8201, "d_p135":  0.0014,
            }

def mag_2_int(mag=1.0, mag_err=0.0):
    intt = 10**(-mag / 2.5)
    intt_err = intt - 10**(- (mag + mag_err) / 2.5)

    return intt, intt_err


def convert_dict(source):
    p000, p000_err = mag_2_int(mag = source["p000"], mag_err = source["d_p000"])
    p045, p045_err = mag_2_int(mag = source["p045"], mag_err = source["d_p045"])
    p090, p090_err = mag_2_int(mag = source["p090"], mag_err = source["d_p090"])
    p135, p135_err = mag_2_int(mag = source["p135"], mag_err = source["d_p135"])

    new_dict = {"name": source["name"], "i000": p000, "i000_err": p000_err,
                "i045": p045, "i045_err": p045_err,
                "i090": p090, "i090_err": p090_err,
                "i135": p135, "i135_err": p135_err,
                }
    return new_dict


all_sources = [bl_lac, bl_lac_1, hd_191195, hd_204827, hd_204827_2, bl_lac_p, cas_p, hd_25443]


for source in all_sources:

    # obtain intensities
    source_intt = convert_dict(source)
    I0 = source_intt["i000"]; I0_err = source_intt["i000_err"]
    I45 = source_intt["i045"]; I45_err = source_intt["i045_err"]
    I90 = source_intt["i090"]; I90_err = source_intt["i090_err"]
```

```python
        I135 = source_intt["i135"]; I135_err = source_intt["i135_err"]

        # calculate U and Q
        Q = (I0 - I90) / (I0 + I90)
        U = (I45 - I135) / (I45 + I135)

        Q_err = 2 / (I0 + I90)**2 * np.sqrt(I90**2 * I0_err**2 + I0**2 * I90_err**2)
        U_err = 2 / (I45 + I135)**2 * np.sqrt(I45**2 * I135_err**2 + I135**2 * I45_err**2)

        PD = np.sqrt(U**2 + Q**2)
        PD_err = np.sqrt((Q**2 * Q_err**2 + U**2 * U_err**2 ) / (Q**2 + U**2))

        PA = np.arctan(U/Q)
        PA_err = np.sqrt((Q**2 * U_err**2 + U**2 * Q_err**2 ) / (Q**2 + U**2)**2)

        print("\n", source["name"])
        print("I0 = ", I0, " +- ", I0_err)
        print("I45 = ", I45, " +- ", I45_err)
        print("I90 = ", I90, " +- ", I90_err)
        print("I135 = ", I135, " +- ", I135_err)
        print("U = ", U, " +- ", U_err)
        print("Q = ", Q, " +- ", Q_err)
        print("PD = ", PD *100, " % +- ", PD_err * 100, " %")
        print("relative deviation: ", PD_err / PD *100, " % ")
        print("PA = ", PA, " rad +- ", PA_err, " rad")
        print("relative deviation: ", PA_err / PA *100, " % ")
```

.3 Patricks code

```python
from lmfit import models, Model
import matplotlib.pyplot as plt
import numpy as np

Mag_cas = np.array([10.9186, 10.9026, 10.9086, 10.8862])
Mag_caserr = np.array([0.0015, 0.0015, 0.0015, 0.0014])

Mag_BL = np.array([14.3198, 14.2275, 14.2669, 14.3922])
Mag_BLerr = np.array([0.0161, 0.016,  0.0157, 0.0176])

Mag_HD = np.array([10.862, 10.9275, 10.87, 10.8201])
Mag_HDerr = np.array([0.0014, 0.0015, 0.0014, 0.0014])

I_cas = 1 * 10**((-Mag_cas) /2.5)
I_BL = 1 * 10**((-Mag_BL) /2.5)
I_HD = 1 * 10**(-(Mag_HD) /2.5)

I_caserr = np.abs(I_cas-10**(-(Mag_cas+Mag_caserr)/2.5))
I_BLerr = np.abs(I_BL-10**(-(Mag_BL+Mag_BLerr)/2.5))
I_HDerr = np.abs(I_HD-10**(-(Mag_HD+Mag_HDerr)/2.5))

for i in range(1,4):

    if i == 1:
        Int = I_cas #I_BL ; I_HD
        Err = I_caserr # I_BLerr ; I_HDerr
    elif i == 2:
        Int = I_BL
```

```python
        Err = I_BLerr
elif i == 3 :
    Int = I_HD
    Err = I_HDerr
else:
        print("WTF?")


Q = (Int[0]-Int[2])/(Int[0]+Int[2])
Qerr = 2/(Int[0]+Int[2])**2*np.sqrt(Int[2]**2*Err[0]**2+Int[0]**2*Err[2]**2)

U = (Int[1]-Int[3])/(Int[1]+Int[3])
Uerr = 2/(Int[1]+Int[3])**2*np.sqrt(Int[3]**2*Err[1]**2+Int[1]**2*Err[3]**2)

PD = np.sqrt(Q**2+U**2)
PDerr = np.sqrt((Q**2*Qerr**2+U**2*Uerr**2)/(Q**2+U**2))

PA = np.arctan(U/Q)
PAerr = np.sqrt((Q**2*Uerr**2+U**2*Qerr**2)/(U**2+Q**2)**2)

print('$', np.round(U,5), '\pm',np.round(Uerr,5), '\pm',np.abs(np.round(Uerr/U,2)),'\% $ &'
```